CHAPTER 2

ONE DIMENSIONAL AMPLITUDE-STEERED ARRAY

The amplitude-steered array, introduced by Hughes and Thompson in 1976 [20], was originally designed to steer a monochromatic signal to a particular direction. Using the array for an imaging application requires an evaluation of the field pattern, the achievable resolution, and the derivation of signal processing methods to form an image. This chapter is concerned with issues of using the linear amplitude-steered array for two-dimensional imaging. The basic operation of the array, an analysis of axial and lateral resolution, and the development of time-frequency processing for forming images are discussed in this chapter. The results presented in this chapter provide the basis for the extension to three-dimensional imaging with the two-dimensional array presented in the next chapter.

2.1 Array Field Pattern

In this discussion, we first consider the one-way far-field pressure of a linear array of equally spaced, equiamplitude point sources. Figure 2.1 gives a diagram defining variables. (All figures and tables appear at the end of the chapter.) To steer the main lobe to θ_0, the signal from each element can be phase-shifted by multiplying by the factor $e^{-j(nk_0d\sin\theta_0)}$, where n is an index used to enumerate the elements, k_0 is the wavenumber at a particular frequency, and d is the distance between the elements. This phase shift will only steer the main lobe to θ_0 at the frequency used to calculate k_0; therefore, a fixed phase shift is generally used for narrowband operation. The

pressure field can be expressed as

$$P(r,\theta) = \frac{e^{-jkr}}{r} \sum_n e^{jnd(k\sin\theta - k_0 \sin\theta_0)} = \frac{Ne^{-jkr}}{r} H(\theta). \tag{2.1}$$

Now, we consider only the array pattern, $H(\theta)$. We assume that we have an array with an even number of elements N, and we measure the phase for each element relative to the center of the array. To simplify the expression, we replace $\frac{kd}{2}\sin\theta$ with u and $\frac{k_0 d}{2}\sin\theta_0$ with ϕ.

$$H(\theta) = \frac{1}{N} \sum_{n=-\frac{N}{2}+1}^{\frac{N}{2}} e^{j(2n-1)(u-\phi)} \tag{2.2}$$

Combining terms of the sum in pairs, we have

$$H(\theta) = \frac{2}{N}[\cos(u-\phi) + \cos(3(u-\phi)) + \cdots + \cos((N-1)(u-\phi))] \tag{2.3}$$

Using the trigonometric identity for the cosine of a sum, Equation (2.3) can be rewritten as

$$\begin{aligned} H(\theta) = \tfrac{2}{N}[&\cos\phi\cos u + \cos 3\phi\cos 3u + \cdots + \cos\left((N-1)\phi\right)\cos\left((N-1)u\right) \\ &+ \sin\phi\sin u + \sin 3\phi\sin 3u + \cdots + \sin\left((N-1)\phi\right)\sin\left((N-1)u\right)] \end{aligned} \tag{2.4}$$

A corresponding equation for an array with an odd number of elements N_{odd} is

$$\begin{aligned} H(\theta) \;=\; \tfrac{2}{N_{odd}} \;&[0.5 + \cos 2\phi\cos 2u + \cos 4\phi\cos 4u \\ &+ \cdots + \cos\left((N_{odd}-1)\phi\right)\cos\left((N_{odd}-1)u\right) \\ &+ \sin 2\phi\sin 2u + \sin 4\phi\sin 4u \\ &+ \cdots + \sin\left((N_{odd}-1)\phi\right)\sin\left((N_{odd}-1)u\right)] \end{aligned} \tag{2.5}$$

Using Equation (2.4), we shift our interpretation of how the beamsteering is achieved. At the beginning of this discussion, we steered the beam by phase-shifting a linear array of equiamplitude elements. Now we steer the beam by weighting the elements. In Equation (2.4), $\cos((2n-1)\phi)$ and $\sin((2n-1)\phi)$ terms are constants which we interpret as amplitude weights on the elements. The $\cos((2n-1)u)$ and $\sin((2n-1)u)$ terms represent combinations of pairs of elements on opposite sides of the center of the array in phase or 180° out of phase, respectively. Therefore, Equation (2.4) can be interpreted as the sum of the outputs of two arrays. The first array

(sum of $\cos(2n-1)u$ terms) combines elements on opposite sides of the center with equal amplitudes and in phase. We call this the phase-symmetric array. The second array (sum of $\sin(2n-1)u$ terms) combines elements on opposite sides of the array with equal amplitudes and 180° out of phase. We call this the phase-antisymmetric array. According to Equation (2.4), the outputs of the two arrays should be added in phase; however, the output of a phase-antisymmetric array is inherently 90° out of phase with the output of a phase-symmetric array. The outputs of the two arrays, therefore, must be added with an additional $\pm 90°$ shift [21]. The sign of the shift determines whether the beam is tilted towards positive θ_0 or towards negative θ_0. We note that if we used only one set of weights, cosine or sine, the beam pattern would have main lobes at both positive θ_0 and negative θ_0.

Conceptually, we have used one array with two sets of weights, or two arrays, to achieve beamsteering. In practice, the array layout is designed such that the phase-symmetric and phase-antisymmetric arrays share the same space. The $\cos(2n-1)\phi$ and $\sin(2n-1)\phi$ factors in Equation (2.4) are the amplitude weights which determine the steering direction of the main beam, but they do not have any effect on sidelobe levels. Further apodization can be applied to achieve reduced sidelobe levels, as demonstrated in Appendix A.

If the array described above is excited by a frequency different from the design frequency used to calculate ϕ, the maximum response will occur at an angle different from the designed steering direction θ_0.

$$\phi = \frac{k_0 d}{2} \sin\theta_0 = \frac{k_f d}{2} \sin\theta_f \tag{2.6}$$

The subscript f was added to k and θ to emphasize that the new steering direction is calculated for a specific frequency f. Rearranging to solve for the new steering direction θ_f gives

$$\theta_f = \sin^{-1}\left(\frac{k_0}{k_f} \sin\theta_0\right) \tag{2.7}$$

which can be restated as

$$\theta_f = \sin^{-1}\left(\frac{f_0}{f} \sin\theta_0\right) \tag{2.8}$$

As the frequency increases, the angle that the beam is steered away from broadside decreases. Table 2.1 lists the steering direction for several frequencies for a 9.76-cm-length array, which is designed to steer to 5° at 5.6 MHz. An example of several beams from the array is shown in Figure 2.2. Beams are shown for 5.6 MHz (5°), 4.5 MHz (6.23°), 3.4 MHz (8.25°), 2.3 MHz (12.25°), and 1.2 MHz (24°). From the table and the figure, we see that as the frequency decreases, the beamwidths increase and the spacing between the beams also increases.

2.2 Resolution Tradeoff for Imaging

We take advantage of the separation of frequencies caused by the amplitude weighting to collect data for a two-dimensional image using a single transmit pulse. A linear-FM chirp is transmitted from the array. As the frequency changes, the main beam is swept over a sector. The reflected wave is received by the array and filtered using a matched-filter to accomplish pulse-compression. Then the short time Fourier transform (STFT) is calculated to determine the range and lateral position of the targets. The one-dimensional amplitude steered array localizes targets using time-of-flight and frequency information. The temporal position of the FFT window gives the range of the target, and the frequencies contained within the window give the lateral position of the target. In this section, we derive the achievable resolution using this scheme.

2.2.1 Definition of resolution

In traditional imaging, where the transducer is shock-excited, axial resolution is determined by the spatial length of the transmitted pulse, which can be related to the relative bandwidth of the transducer and the wavelength at the center frequency and which is independent of the size of the transducer [22].

In analyzing the resolution achieved by the amplitude-steered array, we will use one-point definitions for lateral and axial resolution, which correspond to measuring the axial and lateral extent of the point spread function. This definition is used in contrast to a two-point definition, which would specify the minimum separation

between two points that allows the points to be distinguished. For the amplitude-steered array of point elements operated at a particular frequency f, the array pattern can be written as

$$H(\theta) = \frac{1}{N} \frac{\sin(\frac{N}{2} kd(\sin\theta - \sin\theta_f))}{\sin(\frac{1}{2} kd(\sin\theta - \sin\theta_f))} \tag{2.9}$$

where $k \sin\theta_f = k_0 \sin\theta_0$. We define lateral resolution as the -3-dB width of the one-way array pattern. The -3-dB points on either side of the maximum are the points where the argument of the periodic sinc is ± 1.3894. We use the expression

$$\frac{N}{2} kd(\sin\theta_{-3dB} - \sin\theta_f) = \pm 1.3894 \tag{2.10}$$

Solving for θ_{-3dB} on each side of the maximum array response,

$$\begin{aligned} \theta^+_{-3dB} &= \sin^{-1}(\sin\theta_f + \frac{0.4423\lambda}{Nd}) \\ \theta^-_{-3dB} &= \sin^{-1}(\sin\theta_f - \frac{0.4423\lambda}{Nd}) \\ \alpha &= \theta^+_{-3dB} - \theta^-_{-3dB} \end{aligned} \tag{2.11}$$

where α is the lateral resolution in degrees.

Axial resolution is defined as the spatial length of the pulse:

$$AR = \frac{ct}{2} \tag{2.12}$$

where c is the speed of sound in the medium and t is the temporal length of the pulse. For conventional imaging, where the transducer is shock-excited, this description of axial resolution can be related to an expression for axial resolution which depends on the wavelength at the resonance frequency and on the Q of the transducer, where Q is defined as 2π times the energy stored at resonance divided by the energy lost per cycle [22]. That expression is given by

$$AR = \frac{Q\lambda}{4} \tag{2.13}$$

An alternate definition of Q, $Q = \frac{f_r}{\Delta f}$, where f_r is the resonance frequency and Δf is measured at half power points, is consistent with the previous definition of Q [23]. Therefore, Equation (2.13) is a definition of axial resolution in terms of the inverse of the relative bandwidth of the transducer.

We seek a definition of axial resolution that is similar in form to Equation (2.13). However, our definition of resolution will not depend on the Q of the transducer, but rather on the inverse of the relative bandwidth of the received signal $\frac{f}{\Delta f}$, which we call Q_{sig}. We transmit a chirp and then apply matched filtering for pulse compression. The output of the pulse compression operation is approximately a sinc if the time-bandwidth product of the received signal is large enough [24]

$$\rho = \frac{\sin(\frac{2\pi\Delta f x}{c})}{\frac{2\pi\Delta f x}{c}}, \tag{2.14}$$

where ρ is the correlation between the received signal and the impulse response of the filter, Δf is the bandwidth of the received chirp, c is the speed of sound, and x is the range which is calculated as $\frac{ct}{2}$ when the array is operated in pulse-echo mode. Pulse compression of a linear FM chirp compensates for the quadratic phase and therefore gives an approximately rectangular band of frequencies with linear phase. In the time domain, this description corresponds to a sinc function. The discussion of whether or not the criterion on the time-bandwidth product has been met is reserved until Section 2.2.2. We use the -3-dB points of ρ to find the axial resolution. The function falls to -3 dB, relative to the maximum, when the argument of the sinc function is equal to ± 1.3894:

$$\frac{2\pi\Delta f x_{-3dB}}{c} = 1.3894 \tag{2.15}$$

We write

$$\frac{2\pi f}{c}\frac{\Delta f}{f}x_{-3dB} = 1.3894 \tag{2.16}$$

and solve for $2x_{-3dB}$, where the factor of 2 accounts for the -3-dB points on each side of the maximum. The expression for axial resolution is

$$AR = 2x_{-3dB} = 0.4423\, Q_{sig}\lambda \tag{2.17}$$

where Q_{sig} is the inverse of the relative bandwidth of the received signal, and λ is the wavelength at the center frequency of the received signal f. Although this expression does not explicitly depend on the length of the array, we will see in the next section, where we discuss the tradeoff between axial and lateral resolution, that Q_{sig} depends on the length through the beamwidth. We could have reduced Equation (2.16) to an

expression for x_{-3dB} that was a function of Δf, rather than a function of both Q_{sig} and λ; however, we prefer to have an expression in terms of the wavelength so we can see how resolution will change with center frequency, rather than with bandwidth.

Note that for good resolution, we would like both θ_{-3dB} and x_{-3dB} to be small. Also, note that while absolute range position of the target is given by the time-of-flight (temporal position of the FFT window), the range resolution depends only on frequency bandwidth. Similarly, lateral position may be given by the center frequency of the returned signal, but lateral resolution is determined by the length of the array in terms of number of wavelengths.

2.2.2 Axial and lateral resolution tradeoff

The amplitude-steered array spatially separates frequencies by virtue of the fixed phase shift used to calculate amplitude weights. If the frequencies could be completely separated, i.e., if the beams were infinitely narrow, a point target within the insonified region would produce a single frequency return, implying that two point targets separated only in range could not be distinguished. In reality, it is possible to distinguish multiple targets in the same direction at different ranges because beams are not infinitely thin, but overlap due to the finite length of the array.

Figure 2.3 conceptually shows the tradeoff between axial and lateral resolution. In parts (a) and (b), the curves plotted show the steering direction versus frequency. The curves are the same for both plots. The error bars indicate the -3-dB beamwidth at each frequency. We can see from the error bars that lateral resolution improves with increasing frequency, as expected. Axial resolution can also be determined from each plot. At a particular steering direction, by observing the range of frequencies that overlap, we can determine the bandwidth at that particular direction. In both parts (a) and (b) of Figure 2.3, the frequencies that overlap at a steering direction of 15° are located between the dashed lines. The extent of the dashed lines along the frequency axis tells us Δf. We know the "resonance frequency," the frequency with the greatest amplitude at 15°, from the curve. Therefore, we can determine the wavelength and Q_{sig}. Axial resolution can be calculated using Equation (2.17).

Figure 2.3(a) shows field characteristics for a 1-cm-length array. If the length of the aperture is increased from 1 cm to 4 cm, the lateral resolution improves, illustrated by the decrease in size of the error bars between Figure 2.3(a) and 2.3(b). However, that decrease in beamwidth implies a decrease in the range of frequencies that overlap in a particular direction, illustrated by the more narrow range between the dashed lines in Figures 2.3(a) than in 2.3(b). Therefore, Q_{sig} increases with increased array length, and the axial resolution is worsened. Therefore, there is a tradeoff between axial and lateral resolution that depends on the length of the array, or equivalently, on the width of the beam at each frequency.

Finite element size may change the beamwidth, which affects Q_{sig} and therefore axial resolution. With finite elements, the overall array pattern of Equation (2.9) is multiplied by the beam pattern of the individual element, which can narrow the main beam, thus improving the lateral resolution and degrading the axial resolution. For an array of rectangular elements, the unsteered beam pattern is given by

$$H(\theta) = \frac{1}{N} \frac{\sin(\frac{Nkd}{2} \sin\theta)}{\sin(\frac{kd}{2} \sin\theta)} \frac{\sin(\frac{ka}{2} \sin\theta)}{\frac{ka}{2} \sin\theta} \tag{2.18}$$

where a is the width of the element. The largest possible width of the element is the center-to-center spacing of the elements ($a = d$), which would give a continuous aperture. If N is large, the expression for the width of the main beam will be dominated by the periodic sinc term, the array pattern. Likewise, if $a \ll d$, the expression for the width of the main beam will be dominated by the array pattern. In the other extreme, if $a = d$ and $N = 2$, the effect of the element size is to double the length of the array compared to the array of two point elements. In that case and in similar cases where N is small and $a \approx d$, the finite element size will have a larger effect improving lateral resolution and degrading axial resolution. In general, the effect will be small for practical imaging arrays.

Finally, when deriving the expression for axial resolution, we made use of an approximation that the output of the pulse-compression operation is a sinc function if the time-bandwidth product is large enough. One numerical value for "large enough" is 100. Whether or not this condition is met depends on the received signal, which

means that it depends on the length of the array and the chirp rate. The bandwidth of the received signal will depend on the range of frequencies that overlap, which has been shown to depend on the length of the array. The chirp rate can be set independently so that the criterion is met. One limit to how slow the chirp rate can be is the most shallow range of interest. The entire transmit pulse must be emitted before any signal is to be received.

2.2.3 Simulation and results

We analyze the tradeoff between axial and lateral resolution for a linear array by simulating the received signal from point targets when the array is used in pulse-echo mode. Three arrays with different lengths are used. The first array has 452 elements with center-to-center spacing of 0.216 mm (9.76-cm-length aperture). For comparison, we also simulate arrays with 694 elements (15-cm-length aperture) and 347 elements (7.5-cm-length aperture), but otherwise similar designs. The amplitude weighting is determined so that the main beam is steered to 5° at 5.6 MHz. The transmitted signal is a linear FM chirp with frequency swept from 1.2 MHz to 5.6 MHz. The targets are placed at 20 m, well beyond the intended maximum range, so that they are in the far field for all steering directions and all array lengths. The angular positions of the targets range from 6° to 24°. The speed of sound is assumed to be 1500 m/s for all simulations. Attenuation is not included. The transducer we simulate has a broadband, low-Q impulse response. The main effect of the transducer's transfer function is to reduce the amplitude of targets away from the resonance frequency of the transducer. Therefore, in the simulations we replace the transducer's impulse response with an impulse.

The operation of the linear amplitude-steered array has been simulated using the Field II program, developed by J. A. Jensen [25], [26]. Figure 2.4 shows three images of six point targets, using the three different arrays. Comparing the images in Figure 2.4, particularly for the targets at the higher steering angles, we can observe the tradeoff in axial and lateral resolution that depends on the length of the array. In order to quantify the tradeoff between axial and lateral resolution, resolutions were measured

from images of point targets. From the image in part (c) of Figure 2.4, we can see that both axial and lateral resolution improve with decreasing steering direction, corresponding to increasing frequency. The images in parts (a) and (b) show the improvement in lateral resolution with decreasing steering direction; however, the improvement in axial resolution with decreasing steering direction may be difficult to appreciate.

In addition to the resolution tradeoff that arises due to the size of the array, there is a tradeoff between axial and lateral resolution due to the processing. The length of the sliding FFT window limits the resolution of targets. A very short FFT window implies poor frequency resolution and therefore poor lateral resolution, but it also implies good time localization and therefore good axial resolution. The FFT window can be increased to improve lateral resolution until the fundamental limit on lateral resolution due to the size of the array is reached, but a long window means poor axial resolution. In parts (a) and (b) of Figure 2.4, the difficulty in seeing the degradation of axial resolution due to the length of the array is a result of the relatively long Hanning window used to form the images. For the two shorter arrays, the window length is longer than the achievable axial resolution for the higher frequency (smaller steering direction) targets.

Lateral and axial resolutions were measured from images formed using different length FFT windows in order to reduce the effect of processing on the measurements, so that we could measure the tradeoff in resolution only due to the size of the array. Axial resolution was measured by setting the window length to be short, 8.333 μs. Lateral resolution was measured by setting the window length to be long, 0.147 ms. The long window length was chosen by increasing the length of the FFT window until the improvement in lateral resolution at 6° was less than 0.5%. The images in Figure 2.4 are formed using a window length of 50.8 μs, which is a compromise between the two extremes.

Measurements were made of the -3-dB beamwidths in the lateral direction and the -3-dB signal length in the axial direction (Table 2.2). For all steering directions, lateral resolution improves with increasing array length, and axial resolution degrades

with increasing array length. Calculated and measured lateral beamwidths and axial resolutions are shown in Figures 2.5 and 2.6, respectively. Calculated beamwidths were found using Equation (2.11). Figure 2.5 shows that beamwidths measured from simulated data agreed with calculated beamwidths to a steering direction of 14°. At higher steering angles, corresponding to lower frequencies, the measured beamwidths were larger than calculated beamwidths. This agreement may be improved by using a longer FFT window. Axial resolution was calculated using Equation (2.17), where Q_{sig} was calculated using the predicted beamwidths for each frequency and assuming that the array had a flat frequency response. If a given steering direction was within the steered -3-dB beamwidth of a frequency f, then f was included within Δf used to calculate Q_{sig}. Figure 2.6 shows that the calculated and measured axial resolutions agreed well. The average Q_{sig} predicted for the 7.5-cm, 9.76-cm, and 15-cm apertures are 27.60 ± 0.094, 35.90 ± 0.021, and 55.18 ± 0.054, respectively. The average Q_{sig} measured for the 7.5-cm, 9.76-cm and 15-cm apertures are 28.5 ± 1.85, 36.1 ± 2.01, and 54.1 ± 5.45, respectively. For a given array length, Q_{sig} remains approximately constant over the band of frequencies used, which by Equation (2.17) means that for a given array length axial resolution depends only on wavelength.

Resolution was also measured in the vertical (out-of-plane) direction for the 452-element, 9.76-cm length array. In the vertical direction, resolution is only dependent on the height of the elements. For the simulation, we assumed the elements were twice as tall as they were wide, or 372 μm tall. Resolution can be predicted using Equation (2.19):

$$\alpha_{v,-3dB} = 2 * \tan^{-1}(0.4423\lambda/D) \tag{2.19}$$

where $\alpha_{v,-3dB}$ is the angle of spreading in the vertical direction, λ is the wavelength, and D is the height of the elements. This equation is derived from the beam pattern of a rectangular element. In the vertical direction and in the far field, the beam is defined by $\mathrm{sinc}(\frac{kD}{2}\frac{x}{z})$, where k is the wavenumber, D is the height of the element, x is the coordinate along the height but at the far-field plane, and z is the axial coordinate perpendicular to the array element. The -3-dB points are found when the argument

of the sinc function is equal to ± 1.3894. $\frac{x}{z}$ is equal to $\tan(\frac{\alpha}{2})$. Values for vertical resolution predicted and measured through simulation are presented in Table 2.3.

2.2.4 Summary of resolution study

The far-field array pattern was derived to show how amplitude-weighting causes frequency separation. Expressions were derived to predict axial and lateral resolution in the far field of the array. The theoretical values were used to show that both axial and lateral resolution were dependent on the length of the array. When operated in broadband mode as in the case for imaging, the axial resolution is directly dependent on the size of the array in terms of wavelength, which is different from the operation of conventional transducers. In fact, resolution in the lateral direction can be traded for resolution in the axial direction by changing the array size.

2.3 Time-Frequency Processing for the Formation of Images

Many time-frequency distributions have been studied for various purposes, each having its own benefits and drawbacks. In sonar imaging, time-frequency distributions have been used to identify targets based on characteristics of the distribution for the reflected signals [27], [28]; however, time-frequency processing has not been used to form an image of the target.

In preceeding discussions of the amplitude-steered array, we used the spectrogram to form images. Although the spectrogram is conceptually simple and easy to program, as the extension of the FFT, there are several drawbacks that make it possibly undesirable as the means for forming the image. In particular, there is an inherent tradeoff between time and frequency resolution, so that an improvement in one direction implies a degradation in the other.

Now we investigate the results for other time-frequency distributions. It is generally accepted that there is no known distribution that is ideal for all cases, but that the best distribution for an application must be chosen based on the properties of the signal and the criteria for the result. We compare five distributions, including the

spectrogram, for a test signal which is a simulated reflection from seven point targets. The distributions we have chosen are the spectrogram, the constant-Q spectrogram [29], the Wigner distribution [30], the smoothed pseudo-Wigner distribution [31], and the Choi-Williams distribution [32]. These distributions are among the most common distributions discussed in the literature.

First, we discuss properties of each of the distributions. In Section 2.3.2, we describe our test signal, and the basis for comparison of each of the distributions. Finally, we give results and conclusions. In the following discussion, the terms *time-resolution* and *frequency-resolution* are used; however, the terms *range-resolution* and *lateral-resolution*, respectively, could easily be substituted.

2.3.1 Time-frequency distributions

Two good reviews of time-frequency distributions and their properties are [31] and [33]. In the field of time-frequency analysis, we generally seek a distribution that describes the intensity of a signal simultaneously in time and frequency. In general, it is considered desirable to be able to integrate over all frequencies to get the instantaneous intensity at time t, and to be able to integrate over all time to get the instantaneous intensity at frequency ω.

Many different distributions exist. In fact, an infinite number of them can be generated by changing the kernel function in the following equation, which describes distributions that are the Fourier transforms of a local autocorrelation function:

$$D(t,\omega) = \frac{1}{4\pi^2}\int\int\int e^{-j\theta t - j\tau\omega + j\theta u}\phi(\theta,\tau)s^*(u-\frac{1}{2}\tau)s(u+\frac{1}{2}\tau)dud\tau d\theta \qquad (2.20)$$

where D is the representation of the signal in the time-frequency plane, ϕ is the kernel, s is the signal in the time domain, and s^* is its complex conjugate. The kernel may depend on time and frequency and may also be a functional of the signal. The distributions generated by different kernels satisfy different desirable properties and they produce different energy concentrations. The properties of a distribution can be

investigated by looking at the kernel.

$$\begin{aligned} \phi(\theta,0)=1 \quad &\Rightarrow \quad \int D(t,\omega)d\omega = |s(t)|^2 \\ \phi(0,\tau)=1 \quad &\Rightarrow \quad \int D(t,\omega)dt = |S(\omega)|^2 \\ \phi(0,0)=1 \quad &\Rightarrow \quad \int D(t,\omega)d\omega dt = 1 \\ \phi(\theta,\tau)=\phi^*(-\theta,-\tau) \quad &\Rightarrow \quad D(t,\omega) \text{ is real.} \end{aligned} \tag{2.21}$$

$S(\omega)$ is the Fourier transform of the signal, $s(t)$. $|s(t)|^2$ and $|S(\omega)|^2$ are referred to as marginal densities. The first two equations give the conditions on the kernel so that the marginal densities are preserved, meaning that the instantaneous energy at a specific time or frequency can be calculated by integrations of the joint distribution through frequency or time, respectively. The third equation indicates that if the kernel is normalized to equal 1 at $(\theta,\tau)=(0,0)$ then the total energy is preserved.

If the kernel is independent of the signal, the distribution given by Equation (2.20) is bilinear in the signal, meaning that the signal enters the equation only twice. Bilinear distributions generally suffer from cross-terms which interfere with the interpretation of the distribution as an image. In our imaging application, we are interested in time and frequency resolution as well as low cross-term levels.

In the following discussion, both continuous and discrete expressions are given for the distributions. Generally, the distributions are formulated in the continuous domain, and discrete formulations are obtained from the continuous expressions. The transition to discrete expression is not unique. In many cases, the discrete distribution is periodic with period π rather than 2π, which is the usual period for a discrete signal. To avoid aliasing, the signal can be sampled at twice the Nyquist rate, or the analytic signal, which is zero for the negative frequency components, can be used to calculate the distribution.

Spectrogram

The STFT is the classic method for studying signals whose spectra vary with time. The spectrogram is computed as the magnitude-squared of the STFT. It is quadratic

in the signal and is given by the expression

$$D(t,\omega) = \left| \frac{1}{\sqrt{2\pi}} \int e^{-j\omega\tau} s(\tau) h(t-\tau) d\tau \right|^2 \tag{2.22}$$

where $h(t)$ is the window function used to calculate the STFT. The spectrogram can be expressed using the form of Equation (2.20), with the kernel defined as

$$\phi(\theta,\tau) = \int h^*(u - \frac{1}{2}\tau) e^{-j\theta u} h(u + \frac{1}{2}\tau) du \tag{2.23}$$

The spectrogram has the advantage that cross-terms are reduced to zero as long as the signal components do not overlap in time. And the spectrogram is a nonnegative definite distribution which leads to easy interpretation as an image. The spectrogram preserves the total energy of the signal if the window is normalized, but it does not preserve the marginal densities.

The time and frequency resolution of the spectrogram are determined by the window h used in the calculation. Different tradeoffs can be made by changing the window shape, although for a given window shape, the time and frequency resolutions are determined by the window length. The window cannot be narrow in both the time and frequency domain, so there is an inherent tradeoff in resolution for the spectrogram. Using a definition of resolution that includes both energy concentration and cross-term level, Jones and Parks showed that with an appropriate window, the resolution of the spectrogram could be better than that of some other distributions, including the Wigner distribution [34]. In our case, we define resolution as the energy concentration and consider cross-terms as an additional issue.

Constant-Q Spectrogram

The constant-Q distribution is a special case of the spectrogram, in which the window length is chosen based on the frequency sample being calculated. The number of cycles in the window is kept constant; therefore, a constant ratio between center frequency and bandwidth can be maintained. The constant-Q character is a better match to our received signals. As shown in Section 2.2.3, we expect our received signal to have a constant-Q quality, so that signals with a high center frequency also

have a wide bandwidth and therefore a short time duration. We expect signals with a low center frequency to have a more narrow bandwidth and therefore a longer time duration.

The expression for the constant-Q spectrogram is given by [29]:

$$D[k] = \left| \frac{1}{N[k]} \sum_{n=0}^{N[k]-1} W[k,n]s[n]exp(-j2\pi Qn/N[k]) \right|^2 \tag{2.24}$$

where s is the signal, $N[k]$ is the number of samples used to evaluate the expression for frequency sample k, $W[k,n]$ is a window function set to a Hamming window, for example, and Q is defined as $\frac{f}{\Delta f}$, where f is the frequency.

Expressed using the form of Equation (2.20), the constant-Q distribution is given by [35]

$$D(t,\omega) = \left| \frac{1}{2\pi} \int s(\tau)h((t-\tau)\frac{\omega}{\omega_0})e^{-j\omega\tau}d\tau \right|^2 \tag{2.25}$$

In the constant-Q spectrogram, cross-terms are reduced to zero unless the signal components overlap in time, as for the conventional spectrogram. However, the constant-Q spectrogram also retains some of the undesirable properties of the spectrogram. There is still a tradeoff between time and frequency resolution that is based on the window length. That tradeoff is quantified by a single value Q, the length of the window in terms of number of cycles.

This distribution has been used to analyze music signals, where chords have a constant distance between component frequencies, when the frequencies are plotted on a log scale [29]. The authors point out that they initially tried to use the FFT algorithm because of its computational simplicity; however, they found that plotting the information versus the logarithm of frequency to conform to the pattern expected from musical notes, they had too much information at high frequencies and too little information at low frequencies. In mapping the data from the linear to the logarithmic domain, at low frequencies they had few linear points corresponding to many logarithmic points. At the high frequencies, the opposite was true. In our imaging application, we plot the results of the FFT calculation versus θ where $\theta = \sin^{-1}(f_0 * \sin(\theta_0)/f)$. For constant frequency spacing which is given by the FFT, we have many points at small steering angles and few points at large steering angles.

If we want constant angular spacing at small steering angles, we have many frequency points to map to few angular points. Conversely, at large steering angles we have few frequency points to map to many angular points.

Wavelet transforms also have the "constant-Q" quality. The wavelet transform is given by

$$W(t,a) = \int s(\tau)\sqrt{a}\gamma^*(a(\tau - t))d\tau \tag{2.26}$$

where $\gamma(t)$ is the analyzing wavelet. This is the time-scale expression for the wavelet transform. In the time-frequency expression, the scale a would be replaced by the ratio of frequency to center frequency of the analyzing wavelet $\frac{f}{f_0}$.

Wigner Distribution

The Wigner distribution has received much attention because it is one of the oldest distributions and because it produces a time-frequency representation with the greatest resolution. But the Wigner distribution also has very high cross-terms. This distribution is given by

$$D(t,\omega) = \frac{1}{2\pi}\int e^{-j\tau\omega}s^*(t - \frac{1}{2}\tau)s(t + \frac{1}{2}\tau)d\tau \tag{2.27}$$

where, as before, s is the signal and s^* is its complex conjugate. The kernel is simply 1, which, from the properties given in Equation (2.21), implies that the distribution preserves the marginal densities and the total energy and that it is real. The Wigner distribution is not necessarily zero when the signal is zero, due to the cross-terms; however, it is zero before the signal starts and after the signal finishes. The distribution can have negative values.

The Wigner distribution is periodic with a period π. Therefore, to produce a representation that is free from aliasing, the signal must either be oversampled by a factor of two, or the analytic signal must be used. Using the analytic signal is beneficial for other reasons beyond avoiding aliasing. Cross-terms appear when two frequency components interfere with each other, which includes positive frequencies interfering with negative frequencies from the same signal. Using the analytic signal will reduce the number of cross-terms since there will no longer be negative frequency components.

The discrete version of the Wigner distribution is given by [31]

$$D(n,k) = \frac{1}{\pi} \sum_{\tau=-L+1}^{\tau=L-1} s^*(n-\tau) e^{-j4\pi k\tau/N} s(n+\tau) \tag{2.28}$$

where the limits are included for practical evaluation of the sum. The total length $2L-1$ should be equal to or longer than the duration of the signal.

Smoothed Pseudo-Wigner Distribution

The smoothed pseudo-Wigner distribution is an attempt to reduce the oscillating cross-terms in the Wigner distribution. The smoothed pseudo-Wigner distribution is given by

$$D(t,\omega) = \int\int g(t-t') H(\omega-\omega') D^{Wigner}(t',\omega') dt' d\omega' \tag{2.29}$$

where g filters in the time direction and H is a filter in the frequency direction. If the filter $g(t)$ is a delta function, the distribution is referred to as the pseudo-Wigner distribution.

Smoothing is applied independently in the time and frequency directions; therefore, we do not have the undesirable connection between the two resolutions as in the case of the spectrogram. Smoothing degrades the resolution in the direction in which it is applied, and the smoothing operation destroys the preservation of the marginal densities. For some smoothing filters, we can get a nonnegative definite distribution, but not with Gaussian filters. Therefore, we must choose between having a nonnegative distribution and preserving the marginal densities.

The discrete version of the smoothed pseudo-Wigner distribution is given by a discrete convolution of low-pass filters and the Wigner distribution in the time and frequency directions.

Choi-Williams Distribution

The Choi-Williams distribution was created to reduce cross-terms while preserving the marginal densities. The Choi-Williams distribution is given by

$$D(t,\omega) = \int e^{-j\omega\tau} \left[\int \frac{1}{\sqrt{4\pi\tau^2/\sigma}} exp\left(-\frac{(\mu-t)^2}{4\tau^2/\sigma} \right) s(\mu+\frac{\tau}{2}) s^*(\mu-\frac{\tau}{2}) d\mu \right] d\tau \tag{2.30}$$

where σ is the parameter used to control the properties of the distribution. Small σ implies more smoothing and reduction of the cross-terms. However, this also leads to greater loss of resolution. The loss of resolution is not independently controlled for the time and frequency directions because only a signal parameter σ is used. The Choi-Williams distribution has the drawback that it is difficult to reduce cross-terms if two signal components occur at the same time or the same frequency [33].

The discrete version of the Choi-Williams distribution is given by Equation (20) of [32]:

$$\begin{aligned} D(n,k) &= 2\sum_{\tau=-\infty}^{\tau=\infty} W_N(\tau) e^{-j2\pi k\tau/N} \times \\ &\quad \sum_{\mu=-\infty}^{\mu=\infty} W_M(\mu) \frac{1}{\sqrt{4\tau^2/\sigma}} exp\left(-\frac{\mu^2}{4\tau^2/\sigma} s(n+\mu+\tau)s^*(n+\mu-\tau)\right) \end{aligned} \tag{2.31}$$

where $W_N(t)$ is a symmetric window that is nonzero in the range $t\,\epsilon\,[-N/2, N/2]$, and $W_M(t)$ is a rectangular window that is nonzero in the range $t\,\epsilon\,[-M/2, M/2]$, effectively reducing the limits on the sums.

2.3.2 Test signal and basis for comparison

The test signal is a simulated reflection from a set of seven point targets received by the amplitude-steered array operated in pulse-echo mode. The point targets are located at (6°, 4.0 m), (9°, 4.01 m), (12°, 4.02 m), (15°, 4.03 m), (18°, 4.04 m), (21°, 4.05 m), and (24°, 4.06 m), where the first coordinate is the angular position and the second coordinate is the range. The transmitted signal is a linear-FM chirp with frequency sweeping from 1.2 MHz to 5.6 MHz. The amplitude-steered array steers the 5.6 MHz signal to 5°. The length of the array is 9.76 cm.

The resolution of different distributions is measured as the -6-dB axial and lateral widths of each point target because the array is operated in pulse-echo mode. The highest level of a cross-term is also compared to the maximum target amplitude in the image. Each distribution is optimized within the limits of the parameters available so that the highest level of a cross-term is 20 dB below the peak and so that the axial and lateral resolutions of the point target at 6° are approximately equal and close to 1 cm.

The criterion for highest level of a cross-term was chosen based on the appearance of the images. Cross-terms above this level may interfere with the interpretation of the image. However, lowering cross-terms causes a blurring of auto-terms. In most cases we do not have the degrees of freedom to control all of these criteria, so subjective evaluation is used to produce the best image.

The respresentation of the signal on the time-frequency plane using these distributions will be taken as an image of the targets. Some of the distributions are not positive definite, which makes their interpretation as images difficult. In the cases where the distribution has negative values, the absolute value is taken before logarithmic compression and display of the images.

2.3.3 Results

The spectrogram was calculated using a Hanning window of 590 points or 28.8 μs. In the constant-Q spectrogram, the number of cycles in the window was set to 141. The Wigner distribution does not offer any parameters to optimize. In the case of the smoothed pseudo-Wigner distribution, the filters in the time and frequency directions were Gaussian in shape. They can be defined by the expression $exp(-t^2/\alpha^2 - \omega^2/\beta^2)$, where α is 3.4 μs and β is 125.7×10^3 rad/s. For the Choi-Williams distribution, the rectangular window W_M was 256 samples long, W_N was also a rectangular window 513 samples long, and σ was 0.75.

Measured lateral and axial widths are presented in Table 2.4. Because of the high cross-terms for the Wigner distribution, measurements for targets at 12° to 21° are made using images with only a single target present at a time. The target at 24° was not measured because it appeared at the edge of the image. The target at 24° was not measured for the Choi-Williams distribution because it was not visible in the image.

The images produced with the spectrogram and constant-Q distributions are shown in Figures 2.7 and 2.8. As expected, the spectrogram and constant-Q distributions did not have any cross-terms. The constant-Q distribution achieved better lateral resolution than the spectrogram, although the spectrogram generally produced

better axial resolution. The constant-Q distribution maintained equal lateral and axial resolution for each individual target, while the spectrogram produced much better axial resolution than lateral resolution for the targets at lower frequencies.

The Wigner distribution has no parameters for smoothing, and therefore the level of the cross-terms could not be reduced. An image formed using the Wigner distribution is shown in Figure 2.9. In the image, only the targets at 6° and 9° could be distinguished from the cross-terms. The Wigner distribution is still of interest as a measure of the achievable resolution. The resolutions presented in the table for targets at larger angles were measured using signals that contained only one target at a time.

The smoothed pseudo-Wigner distribution produced the best image of the distributions compared here in terms of combined lateral and axial resolution. The lateral resolutions were comparable to those of the constant-Q distribution, but the axial resolutions were smaller, by a factor of 2 in most cases. And the cross-terms were reduced to an acceptable level. An image is shown in Figure 2.10.

The Choi-Williams distribution was not able to match the performance of the smoothed pseudo-Wigner distribution. An image is shown in Figure 2.11. The Choi-Williams distribution suffers from the drawback that if two components with the same frequency are present at different times, or if two components with different frequencies are present at the same time, the cross-terms are difficult to remove [33]. In our case, the two targets at the lower frequencies overlap enough in time and frequency that the cross-term between them could only be lowered below 20 dB at the cost of great loss in resolution. Therefore, some of the cross-terms were allowed to remain in the image at higher levels. With only one parameter to control time and frequency smoothing and to control the cross-terms, we were unable to effectively trade axial resolution for better lateral resolution.

2.3.4 Summary of the time-frequency study

The performances of several time-frequency distributions were compared using a test signal, which represented a pulse-echo signal from seven point targets. By

moving from the spectrogram to other time-frequency distributions, we have shifted from a tradeoff in axial and lateral resolution to a tradeoff in axial resolution, lateral resolution, and cross-term level. The smoothed pseudo-Wigner distribution gave the best results, most likely because it had the most available parameters. Cross-terms were present at low levels. All of the distributions discussed here have kernels that are independent of the signal. Signal-dependent kernels may give better overall resolution, and they can be designed to give positive definite distributions while still satisfying the marginals.

2.4 Conclusions

The operation of the linear amplitude steered array has been described. The beam pattern has been given, and the use of the array for imaging has been described. A study of axial and lateral resolution has shown that both are dependent on the length of the array, and one resolution can be traded for the other by changing the length of the array. The data processing has also been studied to show that different time-frequency distributions will produce very different images. The smoothed pseudo-Wigner distribution gives the best overall resolution with reasonable cross-terms.

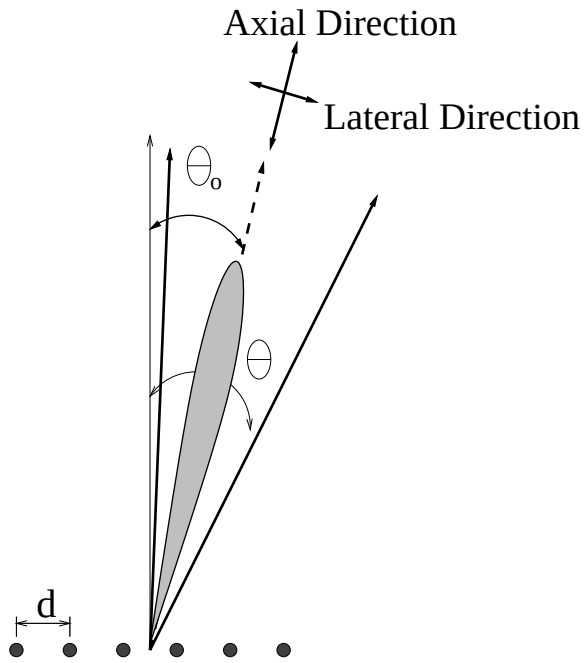

Figure 2.1: Diagram used to define variables for the derivation of the array field pattern.

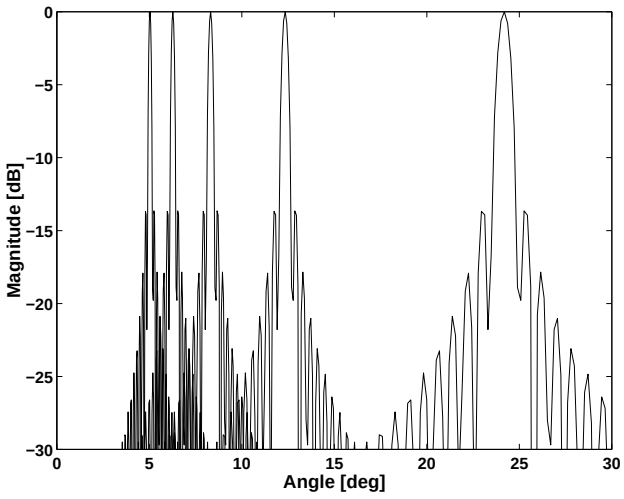

Figure 2.2: Beams from a 9.76-cm aperture steered to 5° at 5.6 MHz. Beams are shown for 5.6 MHz (5°), 4.5 MHz (6.23°), 3.4 MHz (8.25°), 2.3 MHz (12.25°), and 1.2 MHz (24°).

Table 2.1: Steering direction and beamwidth for a 9.76-cm, 452-element array designed to steer to 5° at 5.6 MHz.

frequency (MHz)	Steering Direction (deg)	Change in Steering Direction (deg)	Beamwidth (deg)
1.2	24.00	–	0.7104
1.5	18.99	5.01	0.5491
1.8	15.73	3.26	0.4496
2.1	13.44	2.29	0.3813
2.4	11.73	1.71	0.3315
2.7	10.41	1.32	0.2933
3.0	9.36	1.05	0.2631
3.3	8.51	0.86	0.2386
3.6	7.79	0.71	0.2184
3.9	7.19	0.60	0.2013
4.2	6.67	0.52	0.1867
4.5	6.23	0.45	0.1741
4.8	5.84	0.39	0.1631
5.1	5.49	0.34	0.1534
5.4	5.19	0.31	0.1448

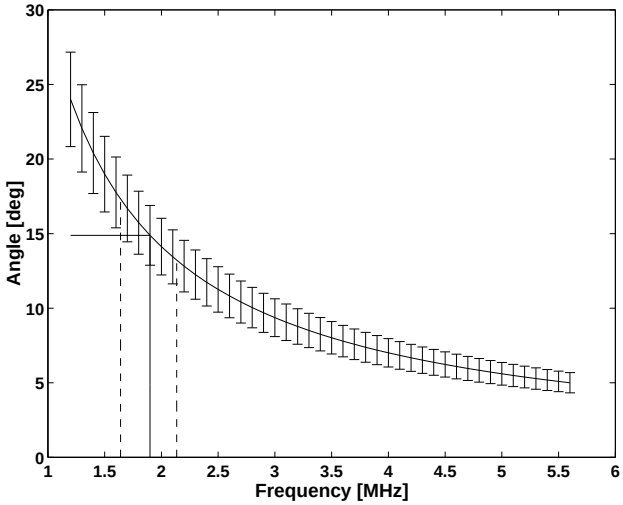

(a)

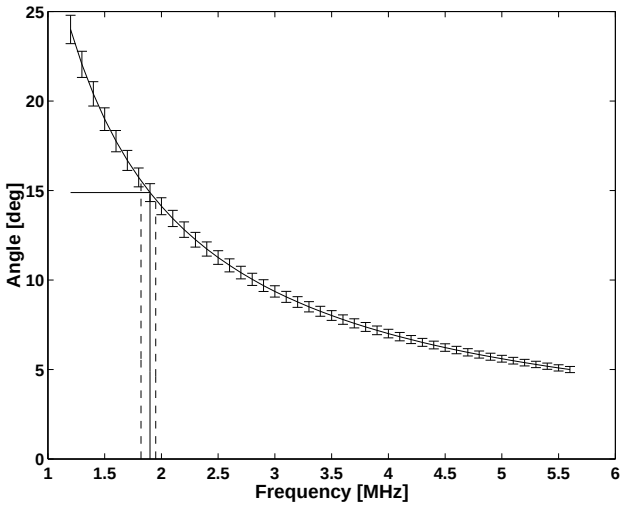

(b)

Figure 2.3: Lateral and axial resolution for (a) 1-cm-length and (b) 4-cm-length apertures. The curve shows the steering direction versus frequency. The errorbars indicate the -3 dB beamwidth at each frequency. The vertical lines indicate how bandwidth decreases when array length is increased.

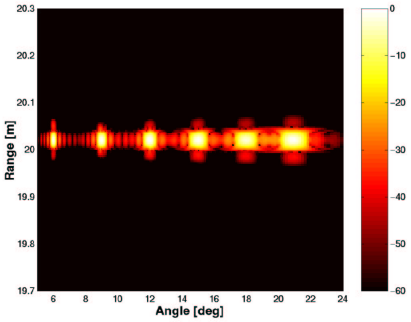

(a)

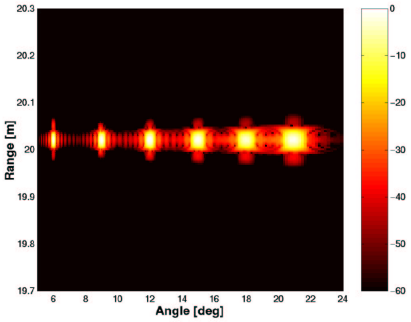

(b)

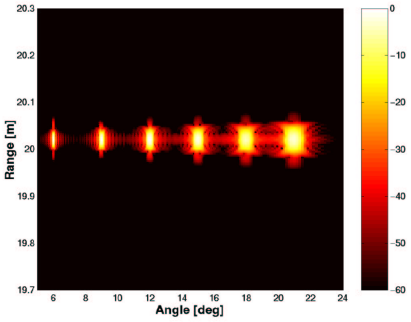

(c)

Figure 2.4: Images formed using simulated reflections from six simulated targets: (a) 7.5-cm, 374-element array, (b) 9.76-cm, 452-element array, (c) 15-cm, 694-element array. Time-Frequency processing is accomplished using the spectrogram with a 50.8-μs Hanning window.

Table 2.2: Axial and lateral resolution measurement results for three array lengths: 7.5 cm, 9.76 cm, and 15 cm. Axial resolution (AR) was measured from images formed using the spectrogram with an 8.333-μs Hanning window. Lateral resolution (LR) was measured from images formed using the spectrogram with a 0.147-ms Hanning window.

angle	6	9	12	15	18	21
f (MHz)	4.669	3.120	2.347	1.886	1.579	1.362
λ (mm)	0.321	0.481	0.639	0.795	0.950	1.10
LR (deg)						
7.5 cm	0.211	0.331	0.404	0.573	0.722	0.808
9.76 cm	0.174	0.254	0.316	0.440	0.539	0.613
15 cm	0.119	0.174	0.214	0.289	0.342	0.421
Δf (kHz)						
7.5 cm	165	110	75	70	60	50
9.76 cm	130	85	60	55	45	40
15 cm	95	55	40	35	30	20
AR (mm)						
7.5 cm	3.845	7.690	8.972	10.25	11.54	15.38
9.76 cm	6.409	8.972	11.54	12.82	15.38	17.94
15 cm	8.972	12.82	16.67	19.23	24.35	26.92

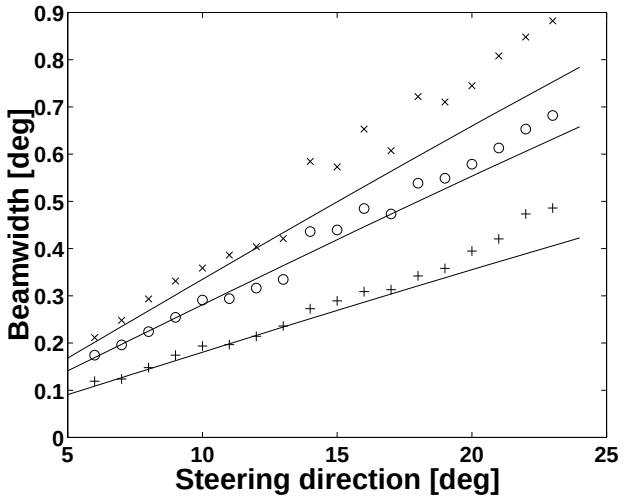

Figure 2.5: Comparison of calculated and measured beamwidths. Measured values are given for 7.5-cm-length array (x), 9.76-cm-length array (o), and 15-cm-length array (+). Calculated values are indicated by the solid lines.

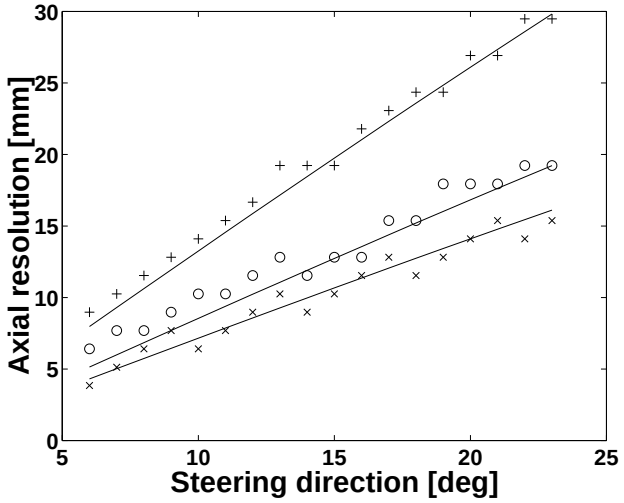

Figure 2.6: Comparison of calculated and measured axial resolutions. Measured values are given for 7.5-cm-length array (x), 9.76-cm-length array (o), and 15-cm-length array (+). Calculated values are indicated by the solid lines.

Table 2.3: Measured and predicted vertical (out-of-plane) resolution for the 452-element, 9.76-cm-length linear array.

Steering Direction (deg)	Predicted Resolution (deg)	Measured Resolution (deg)
6	41.8	44
9	59.5	60
12	74.4	76
15	86.8	92
18	96.9	100
21	105.3	110

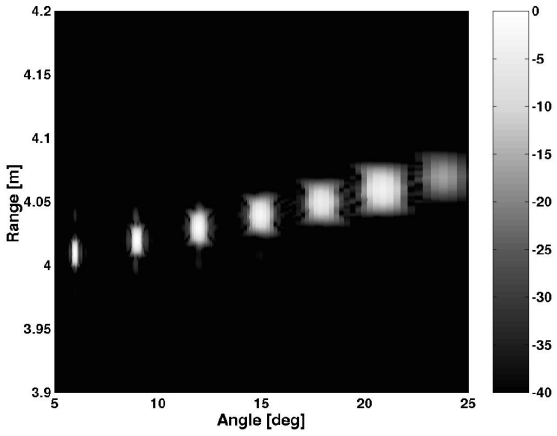

Figure 2.7: Image produced using the spectrogram. The spectrogram was calculated with a Hanning window of 590 points or 28.8 μs.

Table 2.4: Axial and lateral resolution measurement results for different distributions.

Lateral Resolution (mm)							
angle (deg)	6	9	12	15	18	21	24
spectrogram	11.8	19.5	30.6	45.7	66.1	81.8	102
constant-Q	11.1	17.2	23.2	31.0	37.6	42.6	48.7
Wigner*	11.1	16.6	21.5	28.4	34.7	38.5	–
SPWD	11.6	17.1	22.9	30.9	38.9	45.8	53.9
Choi-Williams	16.8	24.9	34.8	51.6	88.9	87.1	–
Axial Resolution (mm)							
angle (deg)	6	9	12	15	18	21	24
spectrogram	11.2	11.2	14.9	16.8	18.7	18.7	24.3
constant-Q	11.0	18.3	23.8	29.3	34.8	40.3	45.8
Wigner*	4.76	8.02	10.2	12.7	14.4	17.7	–
SPWD	7.07	9.41	12.2	14.1	16.0	19.0	21.4
Choi-Williams	7.10	9.89	13.0	14.8	15.6	20.6	–

*Values for Wigner distribution were measured using images with one target present at a time.

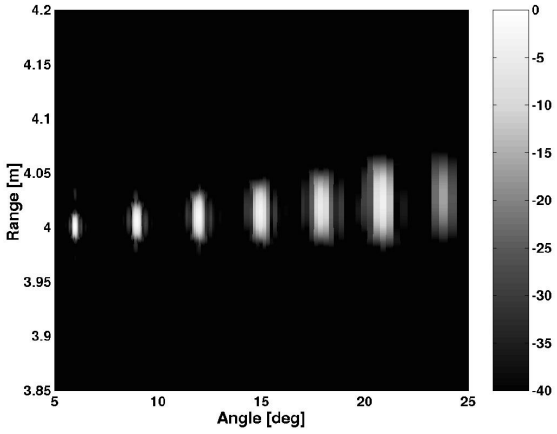

Figure 2.8: Image produced using the constant-Q spectrogram. The constant-Q spectrogram was calculated with a Hanning window containing 141 cycles.

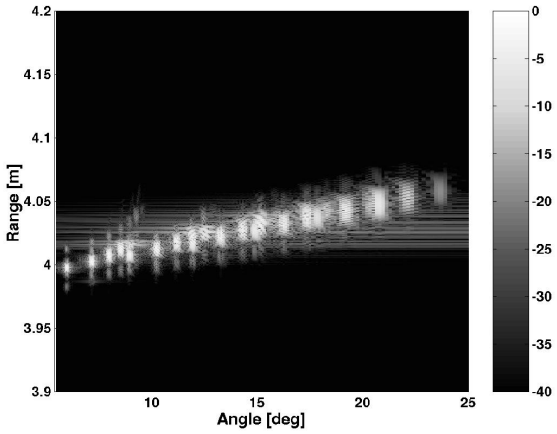

Figure 2.9: Image produced using the Wigner distribution. There were no parameters available for the optimization.

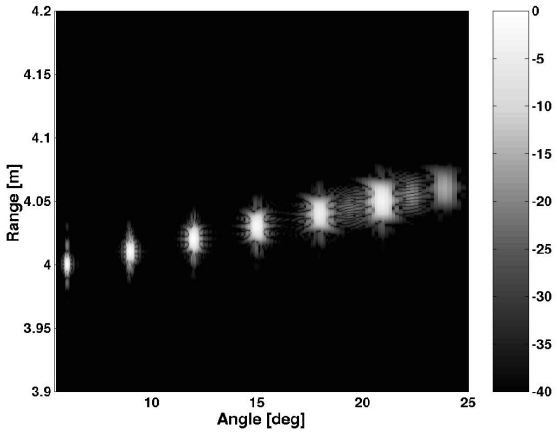

Figure 2.10: Image produced using the smoothed pseudo-Wigner distribution. Smoothing in both time and frequency directions was accomplished using filters with Gaussian shape, $\alpha = 3.4$ μs and $\beta = 125.7 \times 10^3$ rad/s.

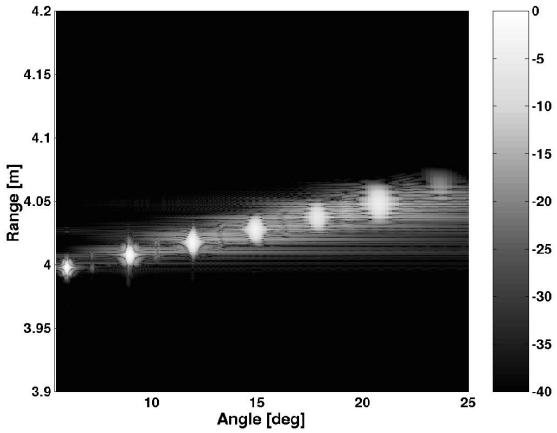

Figure 2.11: Image produced using the Choi-Williams distribution, $\sigma = 0.75$.